



Research article

# Enhanced high-temperature strength of HfNbTaTiZrV refractory high-entropy alloy via Al<sub>2</sub>O<sub>3</sub> reinforcement



Bingjie Wang<sup>a</sup>, Qianqian Wang<sup>a,b</sup>, Nan Lu<sup>c</sup>, Xiubing Liang<sup>c,\*</sup>, Baolong Shen<sup>a,\*</sup>

<sup>a</sup> School of Materials Science and Engineering, Jiangsu Key Laboratory for Advanced Metallic Materials, Southeast University, Nanjing 211189, China

<sup>b</sup> School of Materials Science and Engineering, Jiangsu Key Laboratory of Advanced Structural Materials and Application Technology, Nanjing Institute of Technology, Nanjing 211167, China

<sup>c</sup> Defense Innovation Institute, Academy of Military Science, Beijing 100071, China

## ARTICLE INFO

### Article history:

Received 10 November 2021

Revised 17 January 2022

Accepted 20 January 2022

Available online 26 March 2022

### Keywords:

Al<sub>2</sub>O<sub>3</sub>-reinforcement

HfNbTaTiZrV

Refractory high-entropy alloy

Interstitial strengthening

## ABSTRACT

Novel composites of HfNbTaTiZrV refractory high-entropy alloy (RHEA) reinforced with 0–4 vol.% Al<sub>2</sub>O<sub>3</sub> particles have been synthesized by vacuum arc melting. The microstructure evolution, compressive mechanical properties at room and elevated temperatures, as well as strengthening mechanism of the composites were analyzed. The HfNbTaTiZrV RHEA reinforced with 4 vol.% Al<sub>2</sub>O<sub>3</sub> displayed excellent phase stability at elevated temperatures. A superior compressive yield strength of 2700 MPa at room temperature, 1392 MPa at 800 °C, and 693 MPa at 1000 °C was obtained for this composite. The improved yield strength resulted from multiple strengthening mechanisms caused by Al<sub>2</sub>O<sub>3</sub> addition, including solution strengthening, interstitial strengthening, grain boundary strengthening, and dispersion strengthening. Besides, the effects of interstitial strengthening increased with temperature and was the main strengthening mechanism at elevated temperatures. These findings not only promote the development of oxide-reinforced RHEAs for challenging engineering applications but also provide guidelines for the design of light refractory materials with multiple strengthening mechanisms.

© 2022 Published by Elsevier Ltd on behalf of The editorial office of Journal of Materials Science & Technology.

## 1. Introduction

In the pursuit of high strength for metallic materials, high-entropy alloys (HEAs) with multiple principal elements have attracted extensive attention as a new class of metallic materials over the past two decades. The high configurational entropy of HEAs contributes to the decreased Gibbs free energy in these alloys, which retards the formation of intermetallics and stabilizes single solid solution phase [1–6]. Among them, refractory HEAs (RHEAs) that contain elements with high melting temperatures exhibit high strength at elevated temperatures and excellent radiation resistance in extreme environment, which are considered as promising materials for high-temperature applications such as shafts and turbines for aeroengines, wing tip leading edge of hypervelocity aircraft [7,8]. Nevertheless, most RHEAs exhibit small ductility at room temperature and/or poor phase stability at high temperature. HfNbTaTiZr RHEA is one of the most thoroughly studied RHEAs with large ductility at room temperature and a small density of 9.9 g/cm<sup>3</sup>, which makes it a potential substitution for

Ni-based superalloy [9–11]. However, HfNbTaTiZr RHEA exhibits a low yield strength of 929 MPa at room temperature, which seriously limits its application. In addition, HfNbTaTiZr RHEA displays thermodynamic instability and phase decomposition at high temperatures. It was found the HfNbTaTiZr alloy annealed at 700 °C for only 2.5 h shows a phase decomposition of the originally body-centered-cubic (BCC) high entropy phase into a NbTa-rich BCC phase and ZrHf-rich hexagonal-close-packed (HCP) phases [12]. Therefore, it is crucial to improve the strength and phase stability of HfNbTaTiZr RHEA. Addition of metallic elements, oxides or oxygen atom has been reported to effectively improve the strength and hardness of HEAs. Firstly, alloying with V element can stabilize BCC phase and refine the grains, and thus leads to improvement of strength [13]. Senkov et al. reported that the addition of V improved the room-temperature yield strength of NbMoTaW RHEA from 1058 to 1246 MPa, and yield strength at 1600 °C was enhanced from 405 to 477 MPa [14]. They also demonstrated that the solution of V in CrNbTiZr HEA nearly doubled the yield strength at 800 °C (from 115 to 259 MPa) [15]. Secondly, the addition of fine-scale oxide particles, including Y<sub>2</sub>O<sub>3</sub>, Al<sub>2</sub>O<sub>3</sub>, and TiO<sub>2</sub>, to produce oxide dispersion strengthened (ODS) alloys is an effective means to improve the strength of alloys at room and elevated temperatures by reducing the grain size and inducing Orowan strengthen-

\* Corresponding authors.

E-mail addresses: liangxb\_d@163.com (X. Liang), blshen@seu.edu.cn (B. Shen).

ing [16–18]. Because of the dispersion of  $\text{Y}_2\text{O}_3$  particles, the grain size of ODS CoCrFeNiMn HEA reduced from 0.8 to 0.4  $\mu\text{m}$ , while the yield strength increased from 1000 to 1200 MPa [19]. Due to typical Orowan strengthening caused by  $\text{Al}_2\text{O}_3$  particles, obvious improvement of the compressive yield strength is achieved in  $\text{Al}_2\text{O}_3$ -CoCrFeMnNi HEA, the yield strength increased from 1180 to 1600 MPa [20]. Thirdly, the addition of oxygen atoms in HEAs can overcome the strength-ductility trade-off through the interstitial strengthening. For example, due to the interstitial strengthening of oxygen atoms in HfNbZrTi HEA, the tensile yield strength increased from 776 to 1110 MPa. Besides, the elongation had nearly doubled, increasing from 14.3 to 27.7% [21].

However, the effect of the combination of above-mentioned three strengthening methods in ODS HEAs is rarely studied, and the contribution of each strengthening mechanism needs to be uncovered. In this work, we introduced V element and  $\text{Al}_2\text{O}_3$  particles into HfNbTaTiZr RHEA by vacuum arc-melting. V element with high melting point is expected to stabilize phase structure and improve the strength of the alloy.  $\text{Al}_2\text{O}_3$  was utilized as supplier for interstitial oxygen atoms to promote the interstitial strengthening and the oxide phases to introduce dispersion strengthening simultaneously. The effects of interstitial oxygen atoms and the nanoscale  $\text{Al}_2\text{O}_3$  particles on the compressive mechanical properties of the HfNbTaTiZrV RHEA at room and elevated temperatures were investigated, the dominant strengthening mechanisms responsible for compressive properties were investigated.

## 2. Experimental

$\text{Al}_2\text{O}_3$ -reinforced HfNbTaTiZrV ingots were prepared with pure metals (purity > 99.99 wt%) and  $\text{Al}_2\text{O}_3$  particles (purity > 99.9 wt%) by vacuum arc-melting in an argon atmosphere.  $x$  vol.%  $\text{Al}_2\text{O}_3$ -reinforced HfNbTaTiZrV ( $x = 0, 1, 2, 3, 4$ ) RHEAs, hereinafter are referred to as HfNbTaTiZrV, 1 vol.%  $\text{Al}_2\text{O}_3$ , 2 vol.%  $\text{Al}_2\text{O}_3$ , 3 vol.%  $\text{Al}_2\text{O}_3$ , 4 vol.%  $\text{Al}_2\text{O}_3$ . Alloy ingots were remelted for more than 6 times to eliminate the composition segregation, and then drop-cast into a water-cooled copper mold with dimensions of  $\Phi 10 \times 60$  mm. The samples for compressive tests were cut into cylinders with 2 mm in diameter and 4 mm in height. The room-temperature compression tests were carried out at a crosshead strain rate of  $1 \times 10^{-3}/\text{s}$  using a Sans 5305 system, while the high-temperature compression tests were performed using a Zwick KAPPA 100 machine with the argon atmosphere. Crystal structure and phase constitution of the alloy was analyzed by X-ray diffractometer (XRD, Bruker D8-Discover) with Cu  $\text{K}\alpha$  radiation in a  $2\theta$  range from 20 to 100°. The atomic structure of samples was analyzed using a transmission electron microscope (TEM, Talos F200X). High angle annular dark field scanning (HAADF-STEM) images were recorded using an annular-type detector with collection semi-angle  $\sim 100\text{--}269$  mrad. Volume fraction of the oxide phase was measured from TEM images by employing a commercial software package (Image-Pro-Plus) by using at least 6 TEM images from different grains. Elemental mappings of the samples were acquired by energy-dispersive spectroscopy (EDS). To prepare the samples for TEM analysis, thin foils were electro-polished to 3 mm in diameter and 50  $\mu\text{m}$  in thickness by a DJ2000 twin-jet unit at around -35 °C by using a mixed solution of 6% perchloric acid, 30% *n*-butyl alcohol, and 64% methyl alcohol. Subsequently, the specimen was ion thinned by using a Gatan 691 iron beam thinner for around 30 min. The electron back-scattering diffraction (EBSD) images were obtained using a field emission scanning electron microscope (SEM, JSM-7800F). Specimens for EBSD analysis with dimensions of  $10 \times 10 \times 1$  mm<sup>3</sup> were electrochemically polished by using a mixed solution of 6% perchloric acid, 30% *n*-butyl alcohol, and 64% methyl alcohol solution at a direct voltage of 30 V at room temperature.

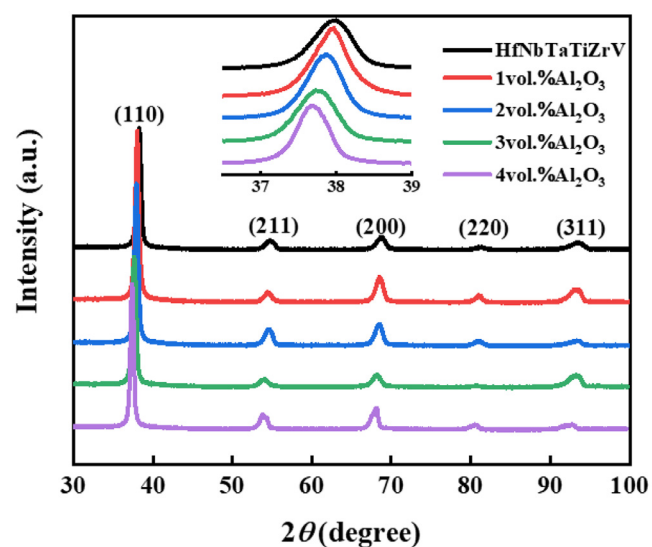


Fig. 1. XRD patterns of the as-cast  $x$  vol.%  $\text{Al}_2\text{O}_3$ -reinforced HfNbTaTiZrV alloys at room temperature.

## 3. Results

### 3.1. Phase identification

The XRD results of the as-cast  $x$  vol.%  $\text{Al}_2\text{O}_3$  reinforced-HfNbTaTiZrV alloys are shown in Fig. 1. All diffraction peaks are indexed to the BCC crystalline structure. As shown in Fig. 1, the peak position of (110) diffraction tends to move towards lower value with the increasing amount of  $\text{Al}_2\text{O}_3$ , indicating that oxygen atoms exist as interstitials in the BCC crystalline lattice. Based on the Rietveld method [22], the lattice parameters of the 0–4 vol.%  $\text{Al}_2\text{O}_3$  alloys are calculated to be 3.359, 3.366, 3.371, 3.377, and 3.381 Å, respectively. The presence of interstitial oxygen atoms increases the crystalline lattice parameter.

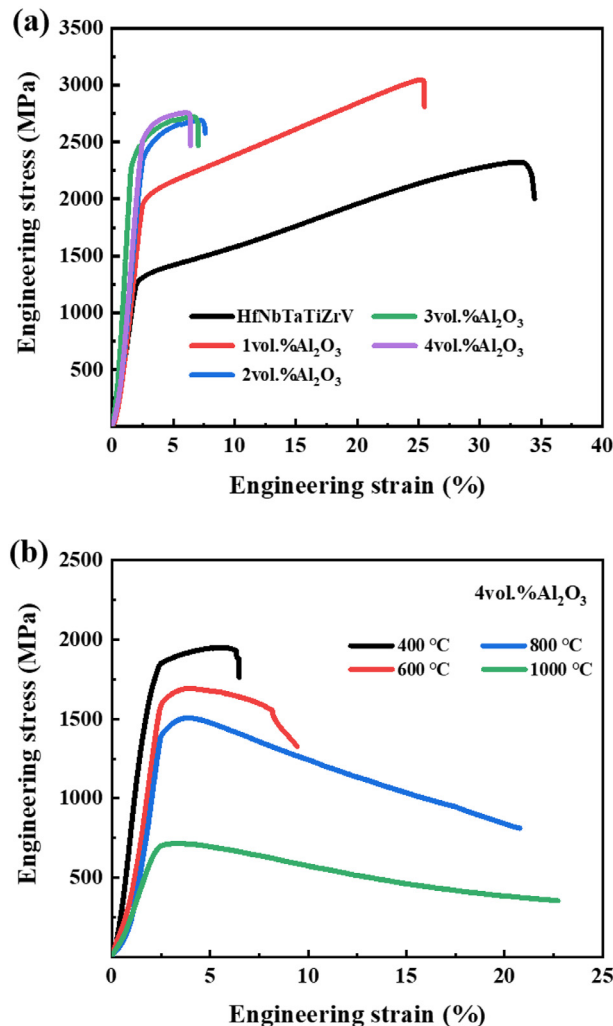
### 3.2. Mechanical properties

Fig. 2(a) shows the room-temperature compressive engineering stress-strain curves of the HfNbTaTiZrV alloys reinforced with 0–4 vol.%  $\text{Al}_2\text{O}_3$  particles. The alloys exhibit work hardening in the compression process. The mechanical properties of the  $\text{Al}_2\text{O}_3$ -reinforced HfNbTaTiZrV alloys are listed in Table 1. The HfNbTaTiZrV alloy exhibits a yield strength of 1300 MPa. With the addition of 1–4 vol.%  $\text{Al}_2\text{O}_3$ , the alloys exhibit a progressive increase in yield strength from 1986 to 2700 MPa. The HfNbTaTiZrV alloy displays 32% plastic strain and the addition of 1 vol.%  $\text{Al}_2\text{O}_3$  do not cause significant reduction in the strain. However, a notable reduction in the plastic strain is observed in  $\text{Al}_2\text{O}_3$ -reinforced samples with content more than 2 vol.% of  $\text{Al}_2\text{O}_3$ . The oxide-reinforced HEAs exhibit higher strength at the expense of the plasticity of the alloy. This is typical mechanical behavior for ODS alloys [23,24]. It is worth mentioning that although the plastic strain of 2–4 vol.%  $\text{Al}_2\text{O}_3$  alloys is small, it still shows work hardening in the deformation process. The work hardening may come from the existence of the interstitial oxygen atom, which improves the critical shear stress necessary for dislocation nucleation and enables an excellent balance in interactions between dislocations and oxygen interstitials, thereby leads to a high strain-hardening reserve [21,25,26]. Thus, the alloys retain plastic deformation ability while the strength is improved.

Since the 4 vol.%  $\text{Al}_2\text{O}_3$  alloy exhibits the highest yield strength at room temperature, it is chosen for elevated temperature com-

**Table 1**Compressive mechanical properties for  $x$  vol.%  $\text{Al}_2\text{O}_3$ -reinforced  $\text{HfNbTaTiZrV}$  alloys at room temperature.

Properties	Alloys					
	$\text{HfNbTaTiZrV}$	1vol.% $\text{Al}_2\text{O}_3$	2vol.% $\text{Al}_2\text{O}_3$	3vol.% $\text{Al}_2\text{O}_3$	4vol.% $\text{Al}_2\text{O}_3$	5vol.% $\text{Al}_2\text{O}_3$
Yield strength (MPa)	1300	1986	2149	2283	2700	2696
Fracture strength (MPa)	2246	3164	2467	2719	2739	2726
Plastic strain (%)	32	22	7	6.5	6	4

**Fig. 2.** Compressive engineering stress-strain curves of (a) the as-cast 0–4 vol.%  $\text{Al}_2\text{O}_3$ -reinforced  $\text{HfNbTaTiZrV}$  alloys at room temperature, (b) 4 vol.%  $\text{Al}_2\text{O}_3$  alloy at elevated temperatures.

pression. The compressive engineering stress-strain curves of the 4 vol.%  $\text{Al}_2\text{O}_3$  alloy at 400, 600, 800, and 1000 °C are shown in Fig. 2(b). The strength of the alloy decreases with the increase of testing temperature. The work hardening phenomenon is kept during compression of the 4 vol.%  $\text{Al}_2\text{O}_3$  alloy at 400 °C. At 600 °C and above, the alloy exhibits obvious dynamic recrystallization, which reaches the maximum strength at the initial stage of deformation, and strain softening occurs in the subsequent deformation [10]. 4 vol.%  $\text{Al}_2\text{O}_3$  alloy shows excellent mechanical properties at high temperatures. The yield strength of 4 vol.%  $\text{Al}_2\text{O}_3$  alloy is 1392 MPa at 800 °C and remains 693 MPa at 1000 °C.

### 3.3. Microstructure characterization

The fracture surfaces of the  $\text{Al}_2\text{O}_3$ -reinforced alloys after compressing at room temperature are shown in Fig. 3. With the incre-

ment of  $\text{Al}_2\text{O}_3$  content, the fracture surface changes from ductile to quasi-cleavage fracture. As shown in Fig. 3(a), the  $\text{HfNbTaTiZrV}$  alloy shows a large number of dimples, which is typical ductile fracture morphology. Fig. 3(b) shows the fracture surface of the 1 vol.%  $\text{Al}_2\text{O}_3$  alloy. Compared with  $\text{HfNbTaTiZrV}$  alloy, the number of dimples decreases and quasi cleavage fracture morphology appears. The dimple morphology disappears and only quasi-cleavage fracture can be observed on the room-temperature fracture surfaces of the 2 vol.%  $\text{Al}_2\text{O}_3$  and 4 vol.%  $\text{Al}_2\text{O}_3$  alloys. As shown in Fig. 3(c, d), similar fracture morphologies are observed in both alloys. The zigzag-shaped fracture surface indicates effective energy dissipation during deformation process, which ensures the alloy has a high strength and 6% plastic strain at the same time [16].

The grain structure of the as-cast  $\text{HfNbTaTiZrV}$  alloys reinforced with 0–4 vol.%  $\text{Al}_2\text{O}_3$  particles characterized by EBSD analysis is displayed in Fig. 4. As shown in Fig. 4(a–e), the grains of  $\text{Al}_2\text{O}_3$  reinforced- $\text{HfNbTaTiZrV}$  alloy are refined with the increasing amount of  $\text{Al}_2\text{O}_3$  apparently. It indicates that the changes in mechanical behavior are partly due to the addition of  $\text{Al}_2\text{O}_3$  particles. The  $\text{Al}_2\text{O}_3$  particles act as barrier for grain boundary migration, which significantly refine the grains. The grains of 4 vol.%  $\text{Al}_2\text{O}_3$  alloys are smaller and more homogeneous (Fig. 4(e)). Fig. 4(f) shows the average grain size of the alloys. It reveals that the alloys consist of equiaxed grains with sizes varying in a wide range from 80 to 13  $\mu\text{m}$ . Since the grain size of the oxide particle is small, both XRD and EBSD results of the alloys show single BCC phase. The oxide phase is characterized by TEM in Fig. 5.

The reason for the change of mechanical properties of the alloys is further uncovered from the TEM analyses. Bright-field TEM images of  $\text{HfNbTaTiZrV}$  and 1 vol.%  $\text{Al}_2\text{O}_3$  alloys are shown in Fig. 5(a, b), respectively. The oxide particles can hardly be observed in the matrix of the 1 vol.%  $\text{Al}_2\text{O}_3$  alloy, probably due to the low oxygen content. TEM images of 2 vol.%  $\text{Al}_2\text{O}_3$  and 4 vol.%  $\text{Al}_2\text{O}_3$  alloys are shown in Fig. 5(c, d), respectively. With the increasing content of oxygen atoms, brittle oxide phases gradually segregate in the alloy. Therefore, the strength increases with the increasing  $\text{Al}_2\text{O}_3$  and the plastic strain decreases at the time.

Taking  $\text{HfNbTaTiZrV}$  and 4 vol.%  $\text{Al}_2\text{O}_3$  alloys as examples, the distribution of oxygen atoms was investigated. HAADF-STEM mapping of the as-cast 4 vol.%  $\text{Al}_2\text{O}_3$  alloy is shown in Fig. 6. Obvious element segregation can be observed in the 4 vol.%  $\text{Al}_2\text{O}_3$  alloy and high content of oxygen atom is detected in the matrix. It indicates that oxygen atom changes the distribution of elements in the alloy matrix. Furthermore, it can be seen from Fig. 6 that some Al atoms are evenly distributed in the matrix. Al atom with an atomic radius of 0.143 nm tends to form substitutional solid solution, which plays the role of solution strengthening and reduces the alloy density [27,28].

Oxygen atom is observed all over the sample, further confirming it exists not only as oxides but also as interstitial solid solution atoms. This explains the phenomenon that the (110) diffraction peak shifts to the left from the XRD results in Fig. 1. To further identify the effects of  $\text{Al}_2\text{O}_3$  addition on the microstructure evolution in the deformation process, bright-field TEM images of  $\text{HfNbTaTiZrV}$  and 4 vol.%  $\text{Al}_2\text{O}_3$  alloys with 5% strain at room temperature are obtained. In Fig. 7(a), low-density dislocation entanglement can be observed in the  $\text{HfNbTaTiZrV}$  alloy, the disloca-

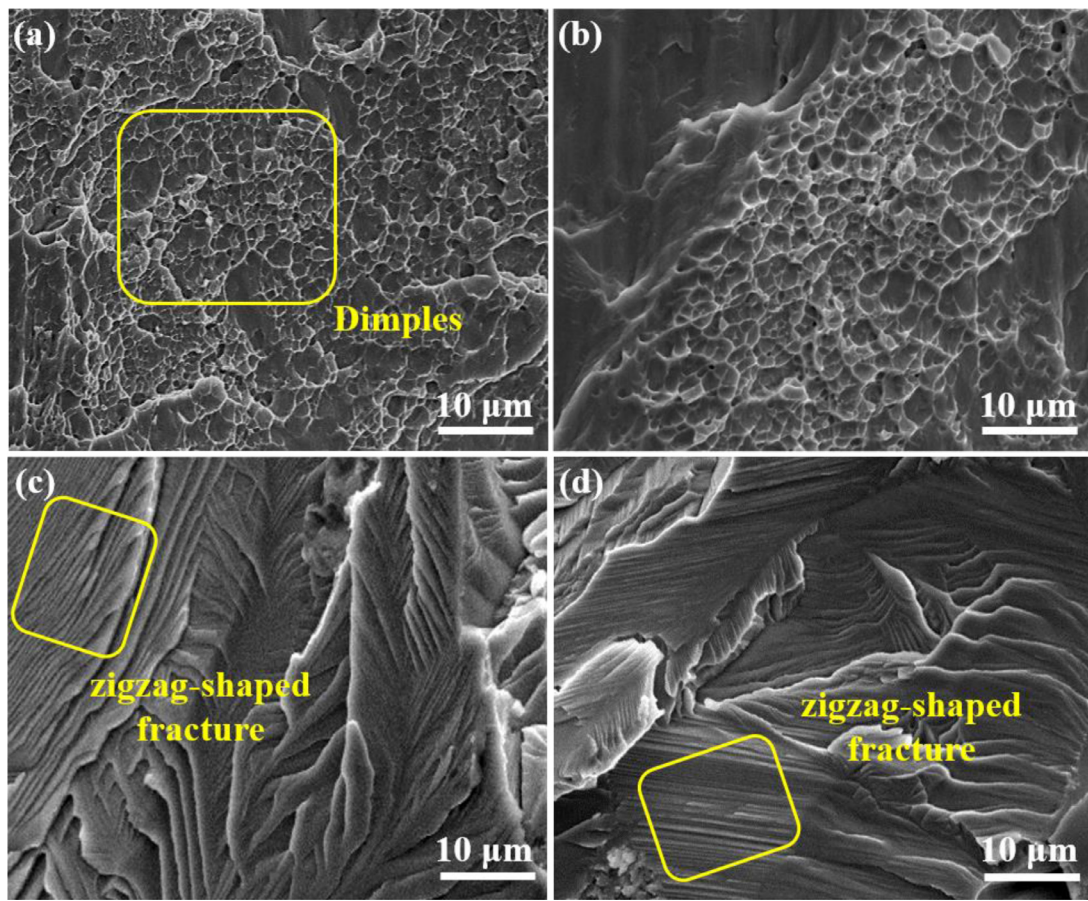


**Fig. 3.** Fracture surfaces of the  $\text{Al}_2\text{O}_3$ -reinforced alloys compressed at room temperature (a)  $\text{HfNbTaTiZrV}$  alloy, (b) 1 vol.%  $\text{Al}_2\text{O}_3$  alloy, (c) 2 vol.%  $\text{Al}_2\text{O}_3$  alloy, (d) 4 vol.%  $\text{Al}_2\text{O}_3$  alloy.

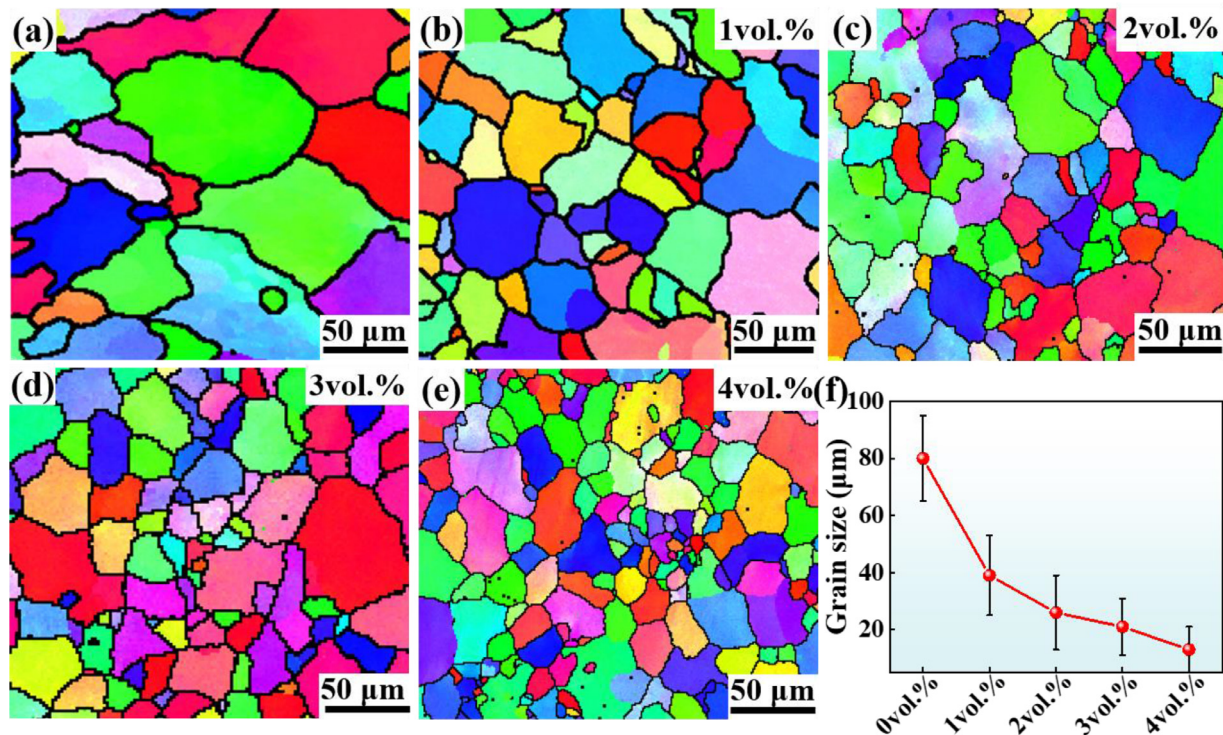


**Fig. 4.** EBSD images of the as-cast  $\text{Al}_2\text{O}_3$ -reinforced  $\text{HfNbTaTiZrV}$  alloys at room temperature (a)  $\text{HfNbTaTiZrV}$  alloy, (b) 1 vol.%  $\text{Al}_2\text{O}_3$  alloy, (c) 2 vol.%  $\text{Al}_2\text{O}_3$  alloy, (d) 3 vol.%  $\text{Al}_2\text{O}_3$  alloy, (e) 4 vol.%  $\text{Al}_2\text{O}_3$  alloy, (f) Average grain size of the alloys.

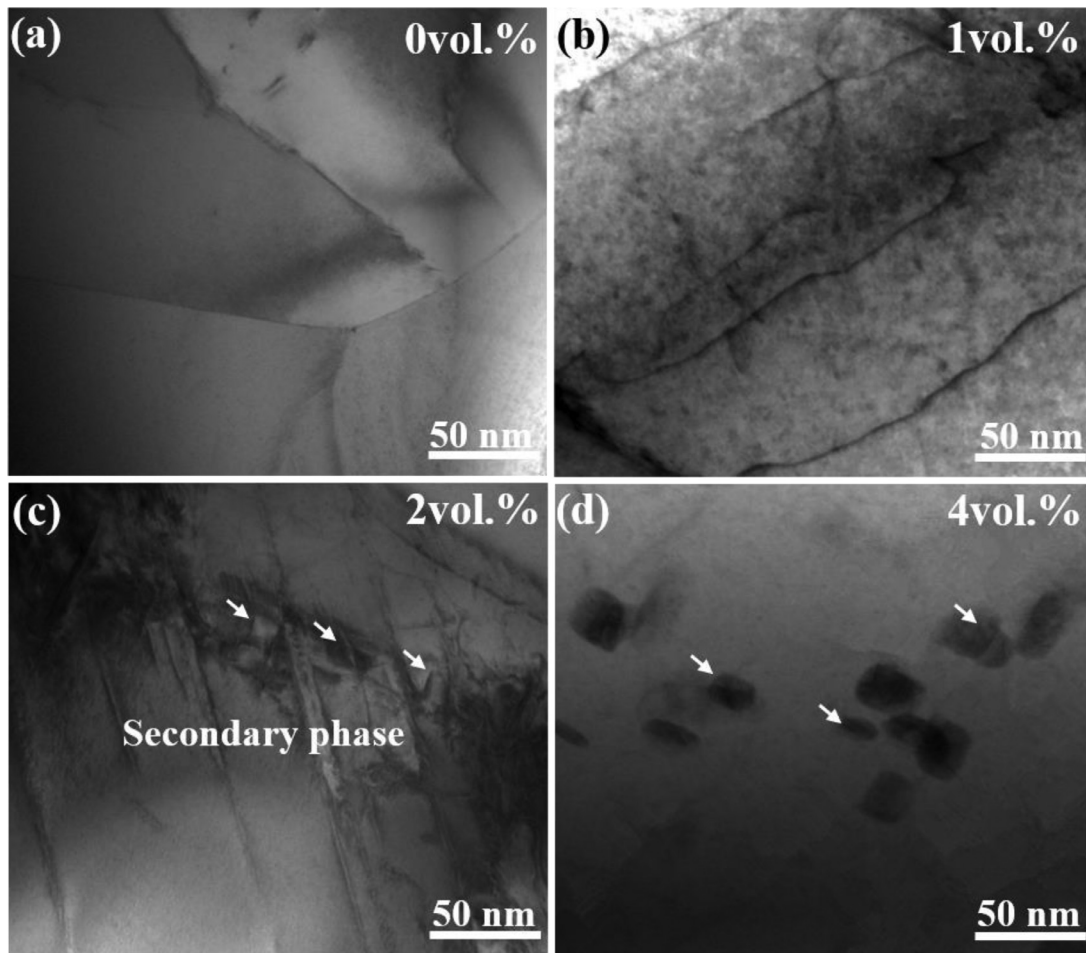


**Fig. 5.** Bright-field TEM images as-cast  $\text{Al}_2\text{O}_3$ -reinforced alloys (a)  $\text{HfNbTaTiZrV}$  alloy, (b) 1 vol.%  $\text{Al}_2\text{O}_3$  alloy, (c) 2 vol.%  $\text{Al}_2\text{O}_3$  alloy, (d) 4 vol.%  $\text{Al}_2\text{O}_3$  alloy.

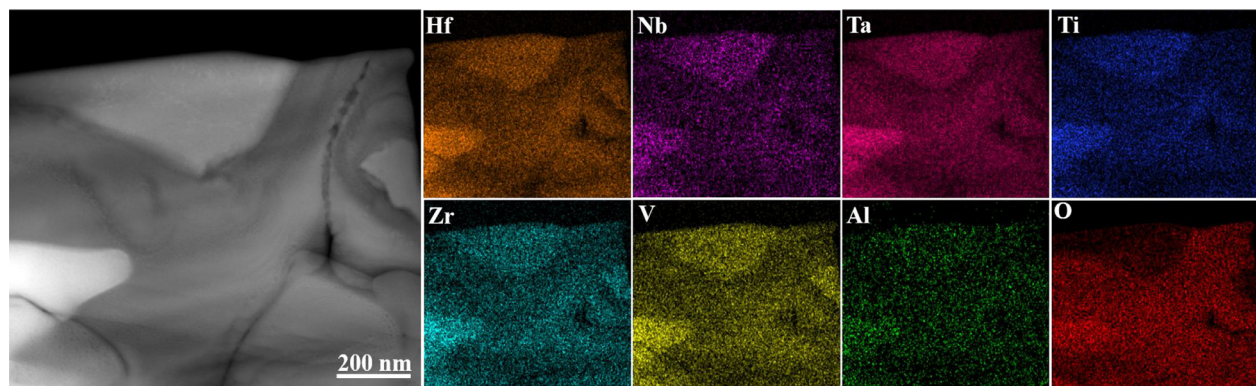


**Fig. 6.** HAADF-STEM micrograph of the as-cast 4 vol.%  $\text{Al}_2\text{O}_3$  alloy along the [110] zone axis (Im-3m) and EDS mappings showing the distribution of elements.

tion motion is dominated by plane slip. The corresponding selected area electron diffraction (SAED) pattern is shown in Fig. 7(b), exhibiting BCC crystalline structure. Multiple ultrafine oxide particles are uniformly distributed in the matrix of 4 vol.%  $\text{Al}_2\text{O}_3$  alloy, pinning and hindering the movement of dislocations during deformation. SAED pattern of the oxide phase in Fig. 7(c) (marked by green arrows) is shown in Fig. 7(d), which reveals that some of the nanoscale particles are  $\text{Al}_2\text{O}_3$  viewed along the zone axis of  $[001]_{\text{Al}_2\text{O}_3}$ . The nanoscale  $\text{Al}_2\text{O}_3$  particles contribute to dispersion strengthening, which is one of the reasons for the increase of yield strength.

Fig. 8(a, b) illustrates the high-resolution transmission electron microscopy (HRTEM) images of  $\text{HfNbTaTiZrV}$  and 4 vol.%  $\text{Al}_2\text{O}_3$  alloys viewed along the [111] direction, respectively. The random distribution of the contrast indicates a random distribution of the constituent elements [29–31]. Inversed Fast Fourier Transform (FFT) images of the  $\text{HfNbTaTiZrV}$  and 4 vol.%  $\text{Al}_2\text{O}_3$  alloys are shown in Fig. 8(c, d), respectively. The 4 vol.%  $\text{Al}_2\text{O}_3$  alloy shows high density of lattice misfits, while no lattice misfit is observed in the  $\text{HfNbTaTiZrV}$  alloy. It confirms that the interstitial solution of oxygen atoms changes the lattice parameters and causes severe lattice distortion [26,32]. To further verify this hypothesis, corre-

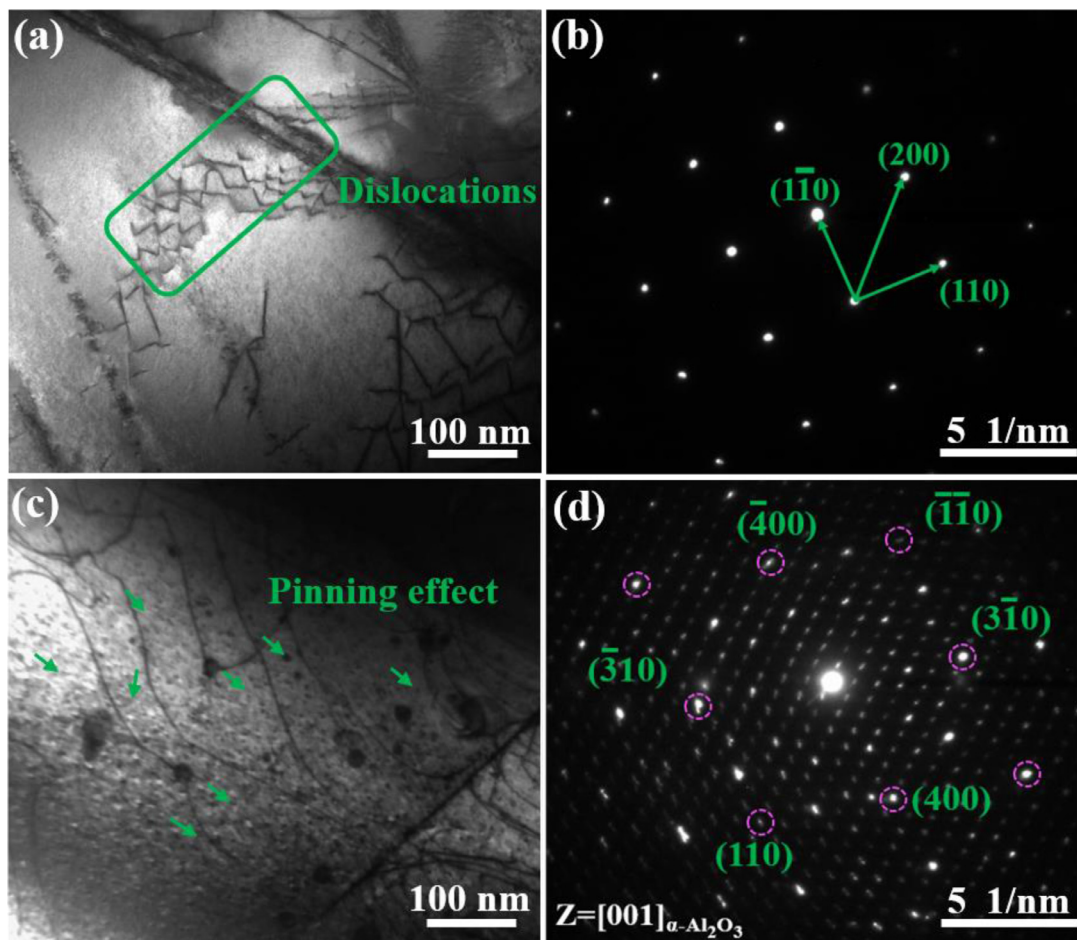


**Fig. 7.** Bright-field TEM images of alloy with 5% strain at room temperature (a) HfNbTaTiZrV alloy, (b) SAED pattern of (a), (c) 4 vol.% Al<sub>2</sub>O<sub>3</sub> alloy, (d) SAED pattern of (c).

sponding mappings of the lattice strains along [121] were determined by using Peak Pairs Algorithm (PPA). As shown in Fig. 8(e, f), the 4 vol.% Al<sub>2</sub>O<sub>3</sub> alloy has a less homogeneous distribution of lattice strains than the HfNbTaTiZrV alloy, revealing higher lattice distortion resulting from interstitials. Besides, as large lattice distortions impose more friction resistance to dislocation migration, the strength of 4 vol.% Al<sub>2</sub>O<sub>3</sub> alloy is improved [26].

To evaluate the phase stability of the Al<sub>2</sub>O<sub>3</sub>-reinforced alloy at elevated temperatures, the XRD diffraction patterns of the alloy after 800 °C compression and annealing at 800 °C for 3 h are shown in Fig. 9(a). It can be seen that the alloys keep the same crystalline structure under two kinds of treatments at 800 °C as the as-cast 4 vol.% Al<sub>2</sub>O<sub>3</sub> alloy. The corresponding bright-field TEM images and SAED pattern viewed along zone axis of [110]<sub>BCC</sub> are shown in Fig. 9(b, c), respectively. Based on the SAED patterns, the phase compositions of the alloys after compressing and annealing at 800 °C are the same as those of as-cast 4 vol.% Al<sub>2</sub>O<sub>3</sub> alloy. It mainly consists of BCC matrix and the Al<sub>2</sub>O<sub>3</sub> particles. No phase decomposition is detected, which indicates that the 4 vol.% Al<sub>2</sub>O<sub>3</sub> alloy exhibits excellent phase stability at 800 °C. EBSD image of the 4 vol.% Al<sub>2</sub>O<sub>3</sub> alloy after 800 °C compression is shown in Fig. 9(d). The coarse grains are observed, which indicates that dynamic recrystallization fully completed at the deformation temperature. It proves that the decrease of yield strength at high temperatures is mainly due to the recrystallization softening [10]. Fig. 9(e) illustrates the polar figures of the 4 vol.% Al<sub>2</sub>O<sub>3</sub> alloy compressed at various temperatures. The corresponding microtextures also changed significantly. The maximum texture intensities of 4 vol.% Al<sub>2</sub>O<sub>3</sub> alloy deformed at room temperature and

400 °C are 7.62 and 6.53 mud, respectively. When the alloy deformed above 600 °C, the preferred orientation of the alloy is evidently weakened by the dynamic recrystallization and the strength is reduced at the same time. This indicates texture strengthening induced by preferred orientation of grains during deformation contributes to the resistance to softening at elevated temperatures. At present, the alloy still has the problem of room temperature brittleness. In the future research, the alloy can be further optimized by adjusting the texture volume fraction by controlling the growth of texture to expand the application of the alloy.

#### 4. Discussion

##### 4.1. Strengthening mechanisms

As revealed by the above analyses, it is inferred that the yield strength of 4 vol.% Al<sub>2</sub>O<sub>3</sub> alloy is improved at room and elevated temperatures by the interstitial strengthening of oxygen atoms, the refined grains, the dispersion strengthening by Al<sub>2</sub>O<sub>3</sub> particles simultaneously. The strengthening mechanisms of the Al<sub>2</sub>O<sub>3</sub>-reinforced HfNbTaTiZrV alloy at room and elevated temperatures can be summarized by four individual parts, including solution strengthening ( $\sigma_{ss}$ ), interstitial strengthening ( $\sigma_{is}$ ), grain boundary strengthening ( $\sigma_{gb}$ ), and the dispersion strengthening ( $\sigma_p$ ). The schematic diagram of the four strengthening mechanisms is shown in Fig. 10(a). In order to determine the contribution of each strengthening mechanism, the yield strength of the 4 vol.% Al<sub>2</sub>O<sub>3</sub> alloy can be calculated as follows [33]:

$$\sigma_{0.2} = \Delta\sigma_{ss} + \Delta\sigma_{is} + \Delta\sigma_{gb} + \Delta\sigma_p \quad (1)$$

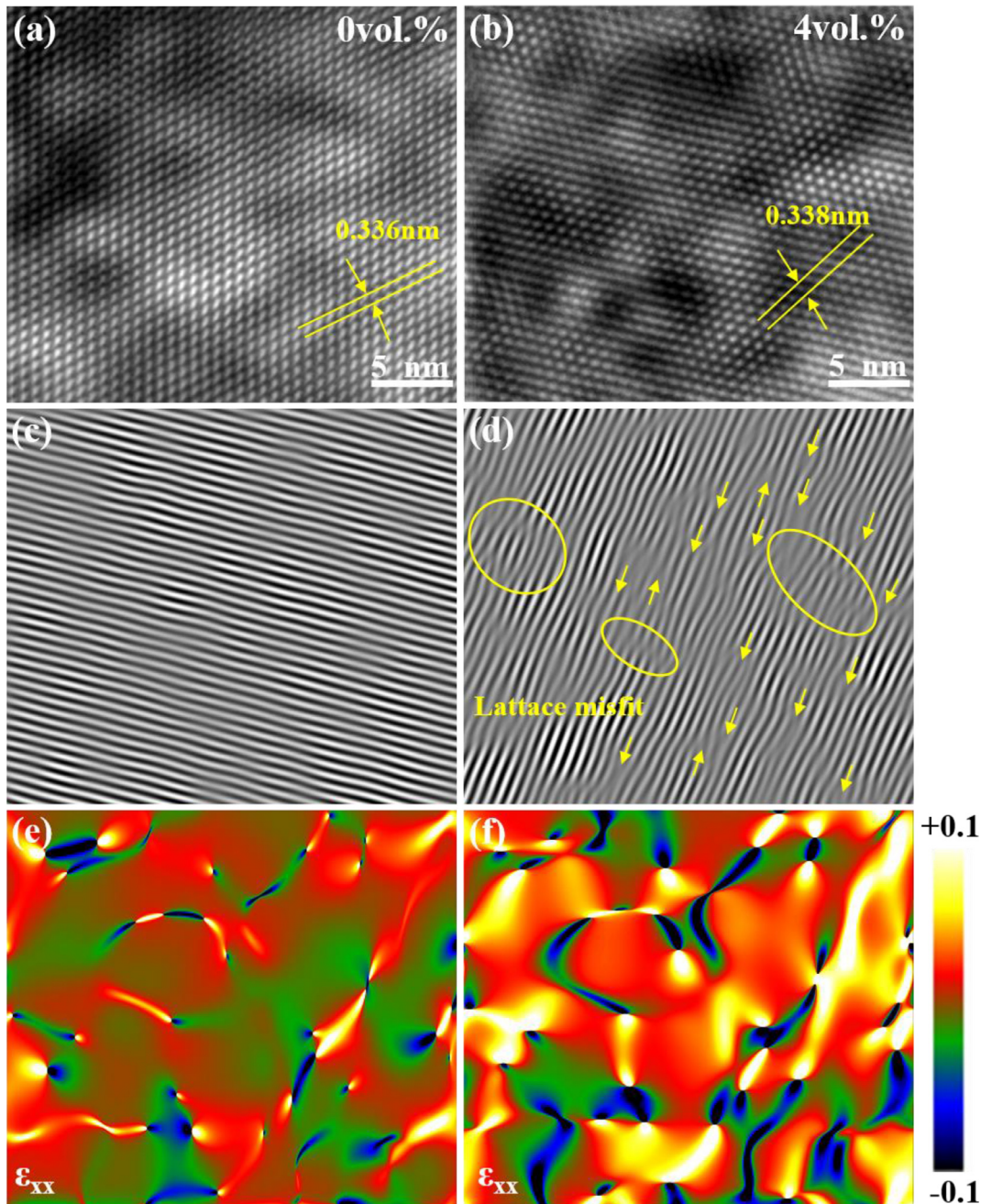


**Fig. 8.** Lattice uniformity analysis of the HfNbTaTiZrV and 4 vol.%  $\text{Al}_2\text{O}_3$  alloy alloys (a) and (b) HRTEM images of the HfNbTaTiV and 4 vol.%  $\text{Al}_2\text{O}_3$  alloys viewed in [110] direction, respectively. (c) and (d) Inversed FFT images of (a) and (b), respectively. (e) and (f) Distribution maps of interatomic distances along [121] in the HfNbTaTiZrV and 4 vol.%  $\text{Al}_2\text{O}_3$  alloys, respectively.

Take the calculation at room temperature as an example,  $\sigma_{ss}$  is the yield strength of the HfNbTaTiZrV alloy coming from solid solution at room temperature (983 MPa), and for 800 °C the value is 364 MPa. According to classical Hall-Petch relationship, the grain boundary strengthening ( $\sigma_{gb}$ ) can be defined as [34]

$$\Delta\sigma_{gb} = \sigma_0 + k_y \frac{1}{d^{1/2}} \quad (2)$$

Here,  $\sigma_0$  is the intrinsic frictional stress offered by the lattice,  $k_y$  is the Hall-Petch coefficient (390 MPa  $\mu\text{m}^{1/2}$ ) [34],  $d$  is the average grain size. The strength increase caused by refined grain size can be derived as:

$$\Delta\sigma_{gb} = k_y \left( d_2^{-1/2} - d_1^{-1/2} \right) \quad (3)$$

In this study,  $d_1$  is the average grain size for HfNbTaTiZrV alloy (80  $\mu\text{m}$ ),  $d_2$  is the average grain size for 4 vol.%  $\text{Al}_2\text{O}_3$  alloy (13  $\mu\text{m}$ ). Therefore, the strength increment caused by the grain boundary is calculated to be 82 MPa.

The increase in yield strength due to  $\text{Al}_2\text{O}_3$  particles is estimated by using Ashby-Orowan relationship [35]:

$$\Delta\sigma_p = M \frac{0.4Gb}{\pi\sqrt{1-\nu}} \cdot \frac{\ln\left(2\sqrt{\frac{2}{3}}r/b\right)}{2\sqrt{\frac{2}{3}}r\left(\sqrt{\frac{\pi}{4f_v}} - 1\right)} \quad (4)$$

Here,  $M$  is the Taylor factor, which is about 3.06 for BCC polycrystalline matrix,  $\nu = 0.373$  is the Poisson's ratio for HfNbTaTiV HEA and is used here as estimates [34].  $G$  is the shear modulus. The Young' modulus of the base HEA is  $128.09 \pm 7.6$  GPa, obtained

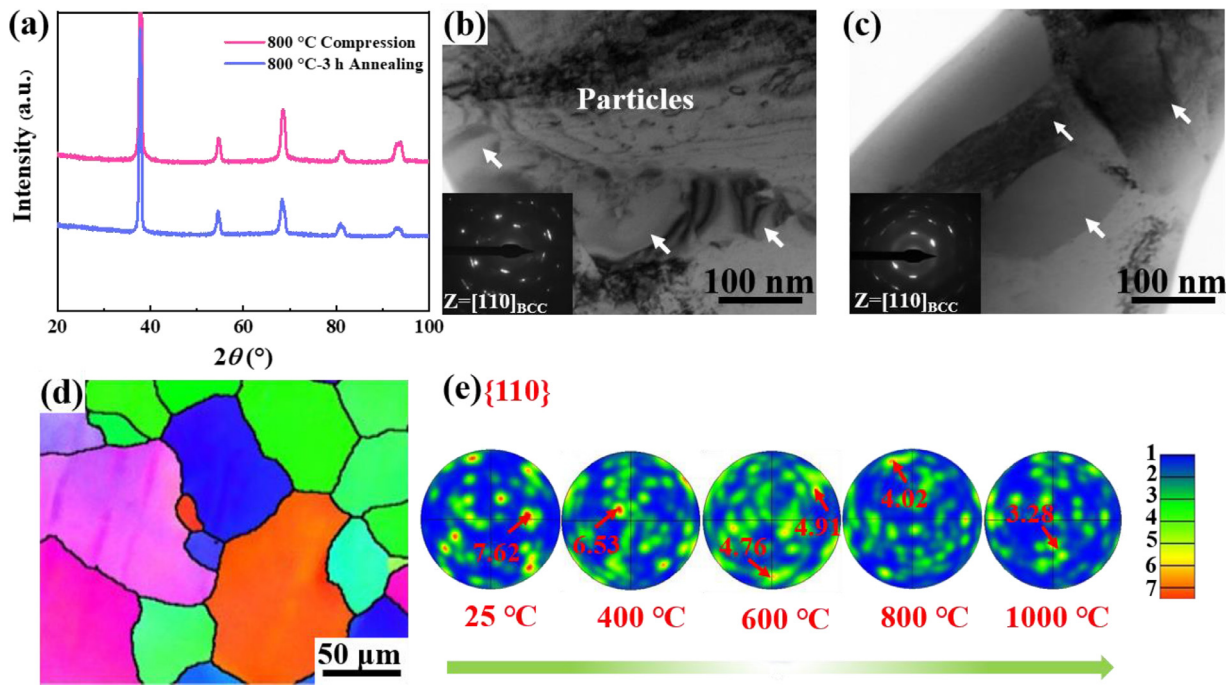


**Fig. 9.** Microstructure of the 4 vol.%  $\text{Al}_2\text{O}_3$  alloy (a) X-ray diffraction patterns of various treatment, (b) Bright-field TEM image of the 4 vol.%  $\text{Al}_2\text{O}_3$  alloy after 800 °C compression, (c) Bright-field TEM image of the 4 vol.%  $\text{Al}_2\text{O}_3$  alloy after annealing at 800 °C for 3 h, (d) EBSD image of the 4 vol.%  $\text{Al}_2\text{O}_3$  alloy after 800 °C compression, (e) Pole figures for  $\{110\}_{\text{BCC}}$  of the 4 vol.%  $\text{Al}_2\text{O}_3$  alloy deformed at various temperatures.

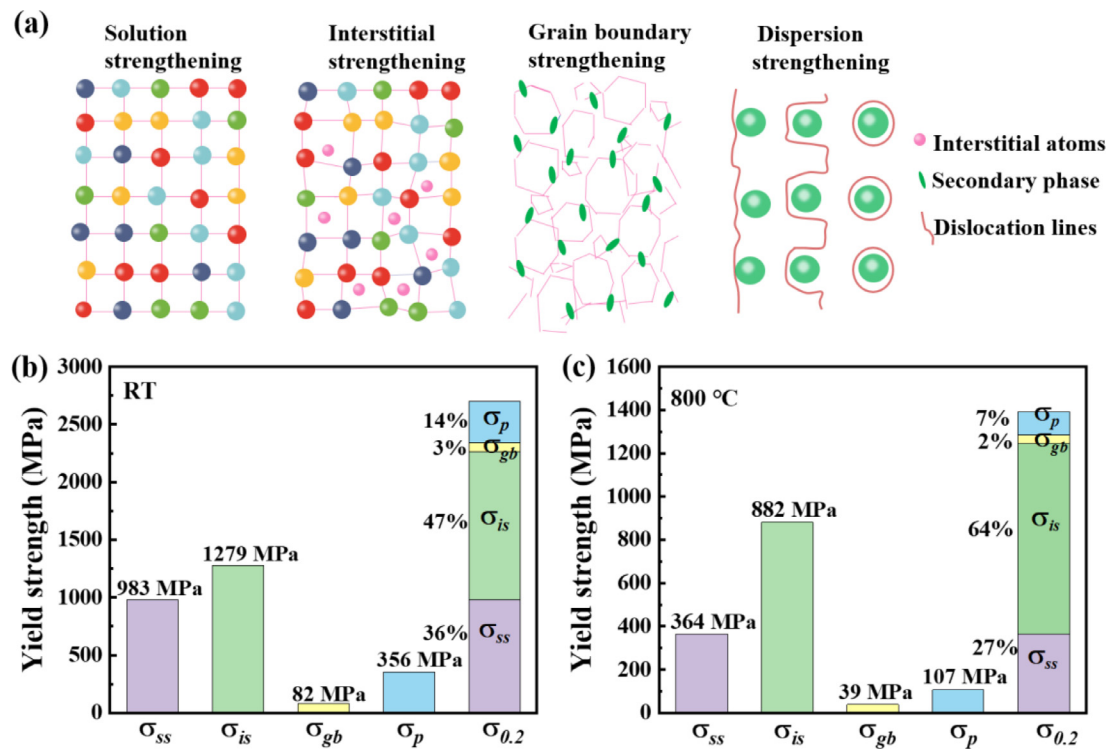


**Fig. 10.** (a) Schematic diagram of the solid strengthening, interstitial strengthening, grain boundary strengthening, and dispersion strengthening, respectively. Contributions of different strengthening mechanisms in the 4 vol.%  $\text{Al}_2\text{O}_3$  alloy during compression at (b) Room temperature and (c) 800 °C.

from compression measurements. The shear modulus is calculated by  $G = E/2(1 + \nu)$ , which is determined to be 56 GPa [21].  $r = 15$  nm is the average radius of  $\text{Al}_2\text{O}_3$  particles.  $f_v$  is the volume fraction of  $\text{Al}_2\text{O}_3$  particles (2.6 vol.% for room temperature).  $b$  is the Burgers vector equals to  $\sqrt{2}a/2$  ( $a$  is the lattice parameter, 3.381 Å).  $\lambda$  is the edge-to-edge distance between particles. Assuming spherical

$\text{Al}_2\text{O}_3$  particles are distributed on a cubic grid, it can be calculated by the following equation [36]:

$$\lambda = 2\bar{\gamma} \left( \sqrt{\frac{\pi}{4f_v}} - 1 \right) \quad (5)$$

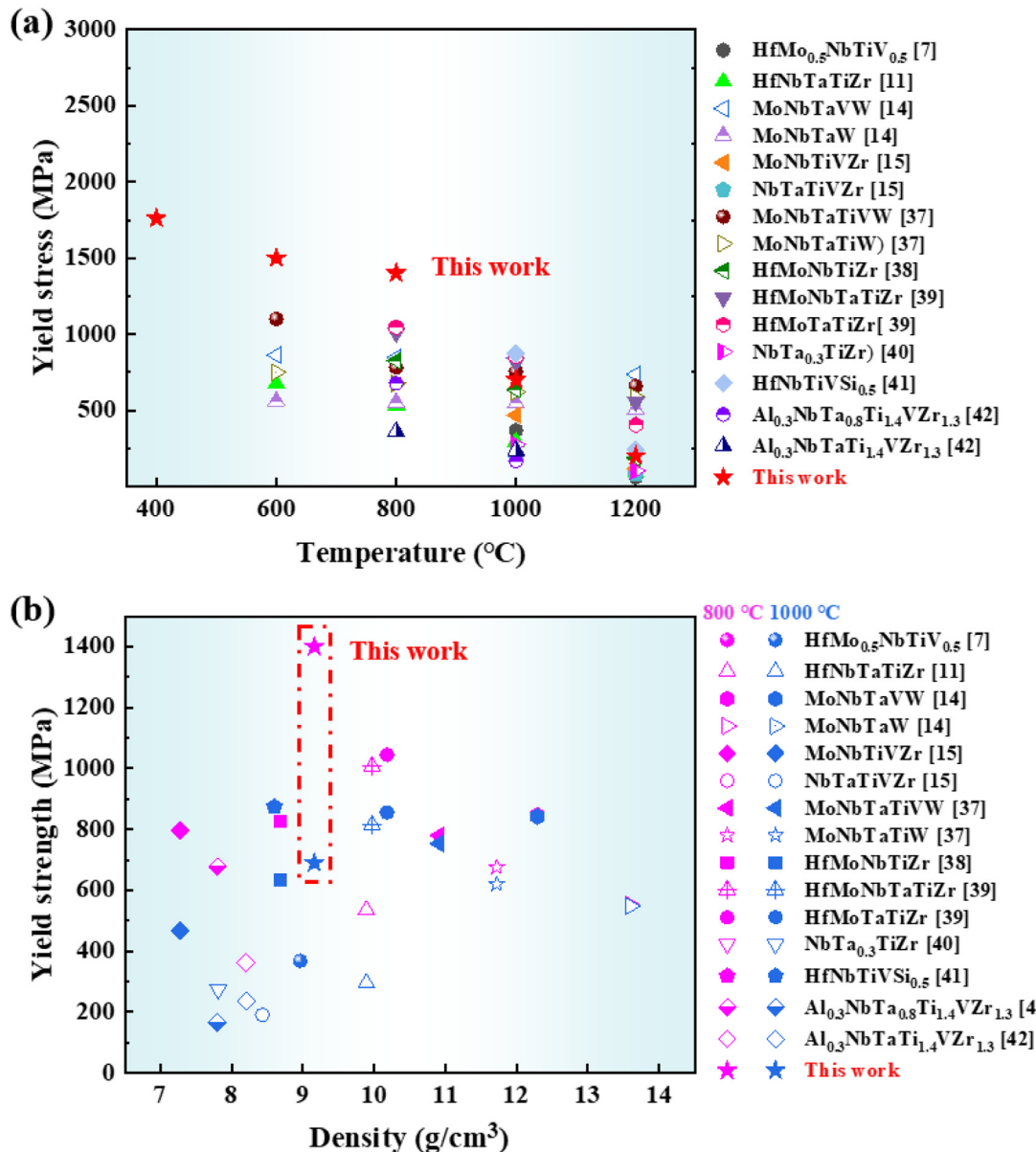


**Fig. 11.** Mechanical property comparison between the 4 vol.% Al<sub>2</sub>O<sub>3</sub> alloy and other RHEAs (a) Temperature dependence on the yield strength, (b) Density-yield strength at elevated temperatures of 800 and 1000 °C.

$\bar{r} = \sqrt{2/3}\gamma$  is the mean radius of a circular cross in a random plane for a spherical oxide phase. Therefore, the increase in yield strength due to Al<sub>2</sub>O<sub>3</sub> phase is calculated to be 356 MPa. Ultimately, the contribution from the interstitial strengthening ( $\sigma_{is}$ ) is determined according to  $\Delta\sigma_{is} = \sigma_{0.2} - \sigma_{ss} - \sigma_{gb} - \sigma_p = 1279$  MPa. The ratios of  $\sigma_{ss}$ ,  $\sigma_{is}$ ,  $\sigma_{gb}$ ,  $\sigma_p$  are 36%, 47%, 3%, and 14%, respectively. Thus, the interstitial solution strengthening plays an important role in improving the strength of the 4 vol.% Al<sub>2</sub>O<sub>3</sub> alloy.

The contribution of various strengthening mechanisms of the 4 vol.% Al<sub>2</sub>O<sub>3</sub> alloy during 800 °C compression at yield strain was calculated by using the same method. Here, we list the detailed parameters for strengthening calculation at elevated temperatures in Table 2. The ratios of  $\sigma_{ss}$ ,  $\sigma_{is}$ ,  $\sigma_{gb}$ , and  $\sigma_p$  for 800 °C compression are 27%, 64%, 2%, and 7%, respectively. The comparison of various strengthening mechanisms at room and elevated temperatures are shown in Fig. 10(b, c), respectively. The results reveal that the contribution of interstitial strengthening exhibits a gradual increase from 47% to 64% in the compressive yield strength

when the experimental temperature increases from 25 to 800 °C, while the dispersion strengthening increases slightly. The reduction degree of each strengthening mechanism, which is defined as  $\delta = (\sigma_{RT} - \sigma_{800\text{ °C}})/\sigma_{RT}$ , is totally different.  $\delta_{ss}$ ,  $\delta_{is}$ ,  $\delta_{gb}$ , and  $\delta_p$  are 64%, 29%, 52%, and 70%, respectively, suggesting the variation of the contribution from different strengthening mechanisms when the temperature changes. Based on the strengthening mechanism calculation, we can infer that interstitial strengthening improves the high-temperature softening resistance of the alloy.

#### 4.2. Mechanical property comparison of RHEAs

Mechanical properties of 4 vol.% Al<sub>2</sub>O<sub>3</sub> alloy at 400, 600, 800, 1000, and 1200 °C are compared with some recently reported RHEAs [7,11,14,15,37–42]. As shown in Fig. 11(a), the 4 vol.% Al<sub>2</sub>O<sub>3</sub> alloy possesses a unique advantage at temperatures above 800 °C. At 800 °C, the yield strength of 4 vol.% Al<sub>2</sub>O<sub>3</sub> alloy is almost three times higher than that of NbMoTaW of 552 MPa,

**Table 2**

Parameters for strengthening mechanism calculation for HfNbTaTiZrV and 4 vol.% Al<sub>2</sub>O<sub>3</sub> alloys during 800 °C compression at yield strain.

Alloy	Grain size $d$ ( $\mu\text{m}$ )	Oxides radius $r$ (nm)	Oxides fraction $f_v$ (%)
HfNbTaTiZrV	203	—	—
4vol.%Al <sub>2</sub> O <sub>3</sub>	50	40	1.9

and is higher by 65% than that of MoNbTaWV alloy of 846 MPa. Even at 1000 °C, it is higher by 26% than that of MoNbTaW of 548 MPa. In addition, comparisons of density and yield strength at 800 and 1000 °C are shown in Fig. 11(b). 4 vol.% Al<sub>2</sub>O<sub>3</sub> alloy has a relatively lower density of 9.26 g/cm<sup>3</sup> and higher strength among the RHEAs. Compared with the high-density alloys such as MoNbTaW (13.61 g/cm<sup>3</sup>) and MoNbTaWV (12.29 g/cm<sup>3</sup>), 4 vol.% Al<sub>2</sub>O<sub>3</sub> alloy displays notable characteristics of lightweight and high-temperature resistance.

## 5. Conclusions

In summary, this work uncovers that proper addition of Al<sub>2</sub>O<sub>3</sub> oxide in HfNbTaTiZrV RHEA strengthened the alloy at room and elevated temperatures. 4 vol.% Al<sub>2</sub>O<sub>3</sub> alloy exhibited a strength of 2700 MPa at room temperature, 1392 MPa at 800 °C, and 693 MPa at 1000 °C. The addition of Al<sub>2</sub>O<sub>3</sub> induced interstitial strengthening, grain boundary strengthening, and dispersion strengthening simultaneously. On one hand, the interstitial solution of oxygen atoms increased the lattice distortion and displayed excellent interstitial strengthening effect. On the other hand, the Al<sub>2</sub>O<sub>3</sub> particles not only pinned at the grain boundary to inhibit the grain growth and refine the grain, but also hindered the movement of dislocation. Dynamic recrystallization was mainly responsible for the decrease of strength at elevated temperatures. Texture was developed and the alloy could be further optimized by adjusting the texture volume fraction. This work reveals the feasibility of adding oxide particles through vacuum arc-melting to improve the mechanical properties and phase stability of RHEAs at elevated temperatures, which broadens the application range of light refractory high entropy alloys.

## Declaration of Competing Interest

The authors report no declarations of interest.

## Acknowledgment

This work was supported by the National Natural Science Foundation of China (Nos. 51975582 and 51631003) and the Jiangsu Provincial Key Research and Development Program (No. BE2021088).

## References

- [1] J.W. Yeh, S.K. Chen, S.J. Lin, J.Y. Gan, T.S. Chin, T.T. Shun, C.H. Tsau, S.Y. Chang, *Adv. Eng. Mater.* 6 (2004) 299–303.
- [2] B. Cantor, I.T.H. Chang, P. Knight, A.J.B. Vincent, *Mater. Sci. Eng. A* 375–377 (2004) 213–218.
- [3] Z.D. Han, H.W. Luan, X. Liu, N. Chen, X.Y. Li, Y. Shao, K.F. Yao, *Mater. Sci. Eng. A* 712 (2018) 380–385.
- [4] S.Y. Wu, D.X. Qiao, H.T. Zhang, J.W. Miao, H.L. Zhao, J. Wang, Y.P. Lu, T.M. Wang, T.J. Li, *J. Mater. Sci. Technol.* 97 (2022) 229–238.
- [5] Q.J. Li, H. Sheng, E. Ma, *Nat. Commun.* 10 (2019) 3563.
- [6] Y. Wu, F. Zhang, X.Y. Yuan, H.L. Huang, X.C. Wen, Y.H. Wang, M.Y. Zhang, H.H. Wu, X.J. Liu, H. Wang, S.H. Jiang, Z.P. Lu, *J. Mater. Sci. Technol.* 62 (2021) 214–220.
- [7] D.B. Miracle, O.N. Senkov, *Acta Mater.* 122 (2017) 448–511.
- [8] Q. Wang, J.C. Han, Y.F. Liu, Z.W. Zhang, C. Dong, P.K. Liaw, *Scr. Mater.* 190 (2021) 40–45.
- [9] B. Gwalani, S. Gorsse, D. Choudhuri, M. Styles, Y. Zheng, R.S. Mishra, R. Banerjee, *Acta Mater.* 153 (2018) 169–185.
- [10] R.R. Eletti, A.H. Chokshi, A. Shibata, N. Tsuji, *Acta Mater.* 183 (2020) 64–77.
- [11] O. Senkov, J. Scott, S. Senkova, F. Meisenkothen, D. Miracle, C. Woodward, *J. Mater. Sci.* 47 (2012) 4062–4074.
- [12] S.Y. Chen, Y. Tong, K.K. Tseng, J.W. Yeh, J.D. Poplawsky, J.G. Wen, M.C. Gao, G. Kim, W. Chen, Y. Ren, R. Feng, W.D. Li, P.K. Liaw, *Scr. Mater.* 158 (2019) 50–56.
- [13] M. Wang, Z. Ma, Z. Xu, X. Cheng, *Scr. Mater.* 191 (2021) 131–136.
- [14] O.N. Senkov, G. Wilks, J. Scott, D.B. Miracle, *Intermetallics* 19 (2011) 698–706.
- [15] O.N. Senkov, S.V. Senkova, C. Woodward, D.B. Miracle, *Acta Mater.* 61 (2013) 1545–1557.
- [16] X. Duan, D. Jia, Z. Wu, Z. Tian, Z. Yang, S. Wang, Y. Zhou, *Scr. Mater.* 68 (2013) 104–107.
- [17] M.Y. Li, Y.H. Guo, W.M. Li, Y.W. Zhang, Y.Q. Chang, *Mater. Sci. Eng. A* 817 (2021) 141368.
- [18] X.C. Wen, Y. Wu, H.L. Huang, S.H. Jiang, H. Wang, X.J. Liu, Y. Zhang, X.Z. Wang, Z.P. Lu, *Mater. Sci. Eng. A* 805 (2021) 140798.
- [19] B. Gwalani, R.M. Pohan, O.A. Waseemc, T. Alam, S.H. Hong, H.J. Ryu, R. Banerjee, *Scr. Mater.* 162 (2019) 477–481.
- [20] Ł. Rogal, D. Kalita, L.L. Dobrzynska, *Intermetallics* 86 (2017) 104–109.
- [21] Z.F. Lei, X.J. Liu, Y. Wu, H. Wang, S.H. Jiang, S.D. Wang, X.D. Hui, Y.D. Wu, B. Gault, P. Kontis, D. Raabe, L. Gu, H.W. Chen, H.T. Wang, J.B. Liu, K. An, Q.S. Zeng, T.G. Nieh, Z.P. Lu, *Nature* 563 (2018) 546–550.
- [22] R.A. Young, *The Rietveld Method*, Oxford University Press, 1993.
- [23] H. Hadraha, Z. Chlup, A. Dlouhy, F. Dobes, P. Roupcova, M. Vilemova, J. Matějicek, *Mater. Sci. Eng. A* 689 (2017) 252–256.
- [24] M. Tane, T. Nakano, S. Kuramoto, M. Niinomi, N. Takesue, H. Nakajim, *Acta Mater.* 61 (2013) 139–150.
- [25] Q.Q. Wei, L.Q. Wang, Y.F. Fu, J.N. Qin, W.J. Lu, D. Zhang, *Mater. Des.* 32 (2011) 2934–2939.
- [26] Y.X. Ye, B. Ouyang, C.Z. Liu, G.J. Duscher, T.G. Nieh, *Acta Mater.* 199 (2020) 413–424.
- [27] J.Y. He, W.H. Liu, H. Wang, Y. Wu, X.J. Liu, T.G. Nieh, Z.P. Lu, *Acta Mater.* 62 (2014) 105–113.
- [28] S.F. Ge, H.M. Fu, L. Zhang, H.H. Mao, H. Li, A.M. Wang, W.R. Li, H.F. Zhang, *Mater. Sci. Eng. A* 784 (2020) 139275.
- [29] Y. Chen, Y. Li, X. Cheng, Z. Xu, C. Wu, B. Cheng, M. Wang, *Mater. Lett.* 228 (2018) 145–147.
- [30] J.A. Smeltzer, B.C. Hornbuckle, A.K. Giri, K.A. Darling, M.P. Harmer, H.M. Chan, C.J. Marvel, *Acta Mater.* 211 (2021) 116884.
- [31] Y.X. Ye, B. Ouyang, C.Z. Liu, G.J. Duscher, T.G. Nieh, *Acta Mater.* 199 (2020) 413–424.
- [32] Y. Liu, G.P. Zheng, M. Li, *J. Alloy. Compd.* 843 (2020) 15606.
- [33] F. He, D. Chen, B. Han, Q. Wu, Z. Wang, S. Wei, D. Wei, J. Wang, C. Liu, J.J. Kai, *Acta Mater.* 167 (2019) 275–286.
- [34] Z.B. An, S.C. Mao, Y.N. Liu, L. Wang, H. Zhou, B. Gan, Z. Zhang, X.D. Han, *J. Mater. Sci. Technol.* 79 (2021) 109–117.
- [35] T. Xiong, S.J. Zheng, J.Y. Pang, X.L. Ma, *Scr. Mater.* 186 (2020) 336–340.
- [36] I. Moravcik, H. Hadraha, L.L. Li, I. Dlouhy, D. Raabe, Z.M. Li, *Scr. Mater.* 178 (2020) 391–397.
- [37] Z.D. Han, N. Chen, S.F. Zhao, L.W. Fan, G.N. Yang, Y. Shao, K.F. Yao, *Intermetallics* 84 (2017) 153–157.
- [38] N.N. Guo, L. Wang, L.S. Luo, X.Z. Li, Y.Q. Su, J.J. Guo, H.Z. Fu, *Mater. Des.* 81 (2015) 87–94.
- [39] C.C. Juan, M.H. Tsai, C.W. Tsai, C.M. Lin, W.R. Wang, C.C. Yang, S.K. Chen, S.J. Lin, J.W. Yeh, *Intermetallics* 62 (2015) 76–83.
- [40] O.N. Senkov, S. Gorsse, D.B. Miracle, *Acta Mater.* 175 (2019) 394–405.
- [41] Y. Zhang, Y. Liu, Y. Li, X. Chen, H. Zhang, *Mater. Lett.* 174 (2016) 82–85.
- [42] O.N. Senkov, D.B. Miracle, K.J. Chaput, J.P. Couzinie, *J. Mater. Res.* 33 (2018) 3092–3128.